PAPER

STORM image denoising and information extraction

Biomedical Physics & Engineering Express

PAPER

STORM image denoising and information extraction

RECEIVED
4 February 2024

REVISED
25 August 2024

ACCEPTED FOR PUBLICATION
12 September 2024

PUBLISHED
24 September 2024

Yuer Lu[1,2,7], **Yongfa Ying**[3,7], **Chengliang Huang**[4], **Xiang Li**[3], **Jinyan Cheng**[1], **Rongwen Yu**[1], **Lixiang Ma**[5], **Jianwei Shuai**[1,2], **Xuejin Zhou**[6] and **Jinjin Zhong**[1,2,*]

[1] Wenzhou Institute, University of Chinese Academy of Sciences, Wenzhou, Zhejiang, 325001, People's Republic of China
[2] Oujiang Laboratory (Zhejiang Lab for Regenerative Medicine, Vision and Brain Health), Wenzhou, Zhejiang, 325001, People's Republic of China
[3] Department of Physics, Xiamen University, Xiamen, 361102, People's Republic of China
[4] Academy of Artificial Intelligence, Zhejiang Dongfang Polytechnic, Wenzhou, 325025, People's Republic of China
[5] Department of Anatomy, Histology & Embryology, School of Basic Medical Sciences, Fudan University, Shanghai, People's Republic of China
[6] College of Mechanical Engineering and Automation, Huaqiao University, Xiamen, 361021, People's Republic of China
[7] These authors contributed equally to this work.
[*] Author to whom any correspondence should be addressed.

E-mail: zjj89@wiucas.ac.cn

Keywords: STORM, image denoising, information extraction, image information clustering

Abstract

Stochastic optical reconstruction microscopy (STORM) is extensively utilized in the fields of cell and molecular biology as a super-resolution imaging technique for visualizing cells and molecules. Nonetheless, the imaging process of STORM is frequently susceptible to noise, which can significantly impact the subsequent image analysis. Moreover, there is currently a lack of a comprehensive automated processing approach for analyzing protein aggregation states from a large number of STORM images. This paper initially applies our previously proposed denoising algorithm, UNet-Att, in STORM image denoising. This algorithm was constructed based on attention mechanism and multi-scale features, showcasing a remarkably efficient performance in denoising. Subsequently, we propose a collection of automated image processing algorithms for the ultimate feature extractions and data analyses of the STORM images. The information extraction workflow effectively integrates automated methods of image denoising, objective image segmentation and binarization, and object information extraction, and a novel image information clustering algorithm specifically developed for the morphological analysis of the objects in the STORM images. This automated workflow significantly improves the efficiency of the effective data analysis for large-scale original STORM images.

1. Introduction

Stochastic optical reconstruction microscopy (STORM) [1–3] is a super-resolution microscopy technique that allows for the application of fluorescence spectroscopy and microanalysis to individual molecules, resulting in a resolution more than ten times higher than conventional optical microscopy [4, 5]. The spatial resolution of traditional optical microscopes is limited by the diffraction of light, causing points to diffract into circular aperture patterns and close points to partially coincide. However, STORM overcomes this limitation by utilizing random interference, thereby improving the resolution by a factor of ten.

This STORM super-resolution technology enables imaging in two or three dimensions, in multiple colors, and can even capture images of living cells [6–8]. The utilization of this imaging technology varies depending on the object of study, the imaging method employed, and the desired image type. It finds application in diverse areas of the life sciences and generates high-resolution images that cater to a wide range of research needs, spanning from neuroscience to subcellular science. Since its introduction, researchers have increasingly recognized the advantages of STORM technology and have incorporated it extensively in their investigations. Notably, STORM has played a pivotal role in various important studies, such as exploring the role of proteins in T-loop formation

in chromatin [9], confirming the reduction of cyanobacterial self-fluorescence in Prochlorococcus spherical us [10], observing the material aggregation around meningococci [11], examining the localization of IFT fusion proteins in cilia [12], investigating the impact of the presence or absence of $\alpha 5$ integrins on spheroid glioma cells [13], and studying the protein chimera composition of RIP1-RIP3 to unveil their role in regulating cell death [14–16].

While STORM offers significant advantages and plays a crucial role in life science, it also has certain insurmountable drawbacks [17, 18] during the imaging process. The imaging capabilities of STORM are constrained by factors such as the microscope optics, the chemical properties of the fluorophore, and the maximum photon exposure permissible for the sample [19, 20]. These limitations necessitate a trade-off between imaging speed, spatial resolution, light exposure, and imaging depth [21, 22]. Under certain experimental conditions, the use of low doses of fluorescent dyes becomes necessary, resulting in a limited number of photons received by the sample. A significant amount of complex noise is generated, which mainly derives from two aspects, quantum shot noise [23] and detector-related noise [24], and obscures valuable information within the image. Quantum shot noise arises as a fundamental characteristic of photon detection, adhering to a Poisson distribution mathematically. This category of noise varies with the signal intensity, leading to elevated noise levels in areas of higher brightness, a consequence attributed to the increase in photon counts. In contrast, detector noise, characterized by a Gaussian distribution [25], affects each pixel uniformly and is independent of the pixel's brightness. Quantum shot noise and detector noise occur independently at the level of individual pixels, without affecting adjacent pixels.

STORM image denoising can be categorized into two approaches: traditional denoising methods and deep learning-based methods. Traditional denoising methods include Non-Local Means (NLM) [26], and Block Matching 3D (BM3D) [27]. The traditional denoising methods are grounded in statistical and algorithmic principles that excel at removing noise patterns that are consistent or pervasive across and image [28]. For instance, NLM works by averaging the value of a pixel with values of similar pixels from other parts of the image, which works well for Gaussian noise where the statistical properties are uniform across the image. BM3D extends this by operating in 3D collaborative filtering groups that can better preserve details while reducing noise. However, these methods are challenged by complex noise structures, especially those found in advanced biological imaging techniques like STORM, due to the non-uniform and signal-dependent character. In contrast, deep learning-based methods utilize training datasets derived from experiments or simulations to learn specific patterns and achieve end-to-end image transformation for effective image denoising [29–35]. Prominent methods in the field of fluorescence microscopy image noise reduction involve supervised training. Examples of such methods include the CARE [19] method proposed by Weigert *et al* in 2018, the Noise2noise [36] method proposed by Lehtinen *et al* in 2018, and the DeepCAD [37] method proposed by Li *et al* in 2021.

Although automatic processing techniques, such as deep learning, have been widely used for many tasks in image processing after denoising, there are still certain specific tasks that necessitate manual selection of target materials for processing. For instance, the extraction of information regarding specific states of proteins requires manual intervention. Within the domain of protein assembly analysis, the task of distinguishing between colocalizing and non-colocalizing clusters remains a manual process [38, 39]. To enhance the efficiency of image processing, it is crucial to develop a comprehensive suite of automated methods for extracting and analyzing information pertaining to specific objects within STORM images. A fully automated image processing pipeline, extending from the initial raw STORM image to the final biological analysis, which includes determining the states of protein aggregation, would significantly boost efficiency in handling and interpreting image data, particularly in high-throughput scenarios. This advancement holds substantial significance for the field of biological imaging research, as it promises to streamline workflows and facilitate more rapid and accurate data analysis. In this study, we devised a workflow for automatic image processing encompassing image denoising, objective image segmentation and binarization, and final image analysis. Our workflow incorporates the previously proposed UNet-Att denoising algorithm, as well as our devised image information clustering algorithm. This integrated approach facilitates an exceptionally efficient denoising capability for the STORM images and the effective ultimate morphological analysis of the substances starting from raw STORM images in a more time-efficient way.

2. Image denoising

2.1. Network design

The network structure of our image denoising algorithm, UNet-Att, is illustrated in figure 1(a). The python packages of UNet-Att are freely available at https://github.com/YongfaYing/UNet_Att. This algorithm is composed of three primary modules: the downsampling module, attention module, and multidimensional upsampling module. The network structure of each module is presented in figures 1(b)–(d). The downsampling module extracts image features at various scales, the attention module enhances the weight of image texture information during fusion, and the multidimensional upsampling module restores image information and combines the output

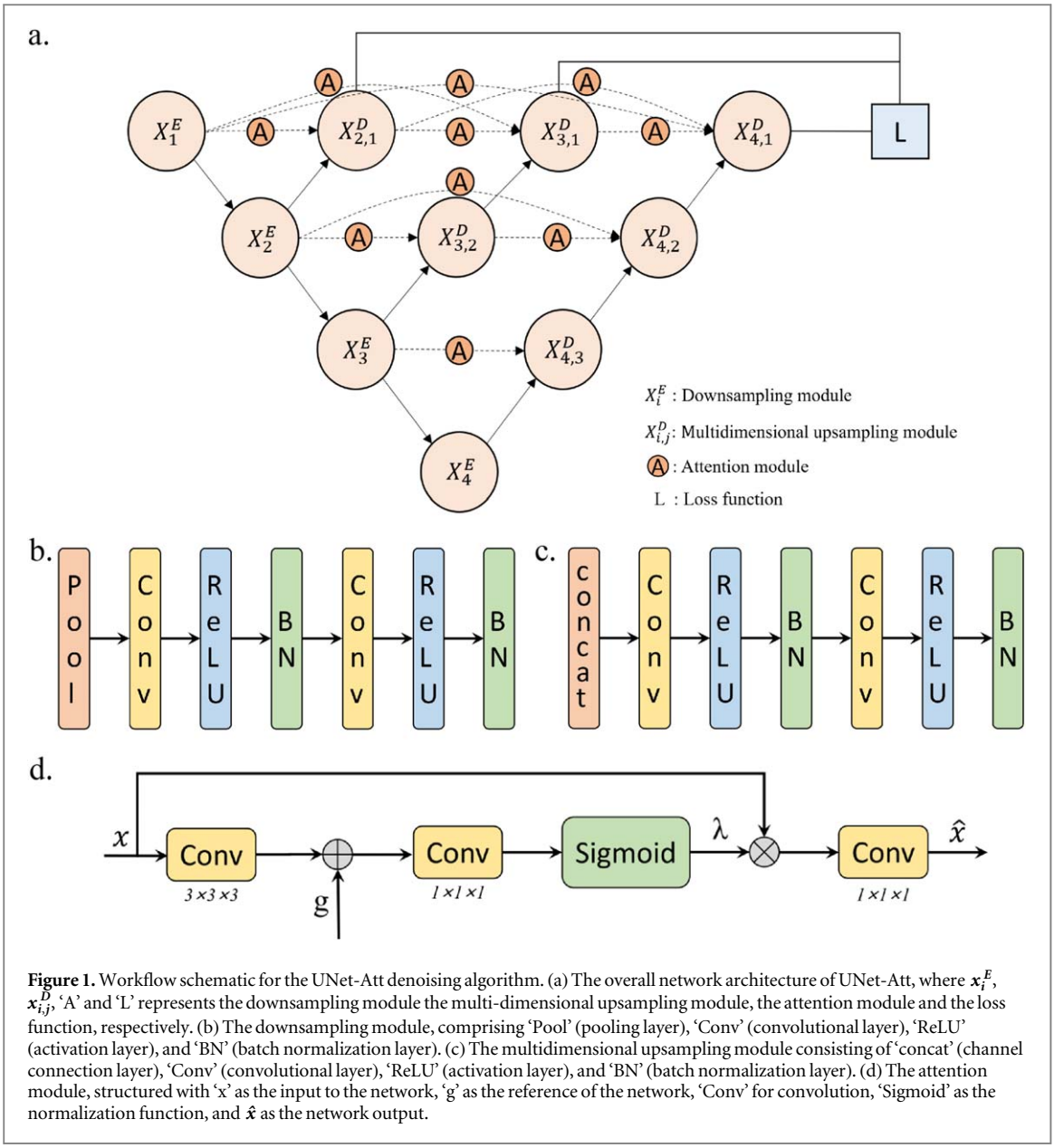

Figure 1. Workflow schematic for the UNet-Att denoising algorithm. (a) The overall network architecture of UNet-Att, where $\boldsymbol{x}_i^E$, $\boldsymbol{x}_{i,j}^D$, 'A' and 'L' represents the downsampling module the multi-dimensional upsampling module, the attention module and the loss function, respectively. (b) The downsampling module, comprising 'Pool' (pooling layer), 'Conv' (convolutional layer), 'ReLU' (activation layer), and 'BN' (batch normalization layer). (c) The multidimensional upsampling module consisting of 'concat' (channel connection layer), 'Conv' (convolutional layer), 'ReLU' (activation layer), and 'BN' (batch normalization layer). (d) The attention module, structured with 'x' as the input to the network, 'g' as the reference of the network, 'Conv' for convolution, 'Sigmoid' as the normalization function, and $\hat{\boldsymbol{x}}$ as the network output.

results of the multidimensional network. This algorithm can effectively remove the image noise while better preserving the original structural texture features in the fluorescent microscopic images. Here, we firstly apply this algorithm to the denoising of the STORM images, and examine its effectiveness.

2.2. Loss function

The loss functions used in this study are the L_1 parametric loss and the L_2 arithmetic mean of the parametric loss. The L_1 loss is defined as the sum of the absolute differences between the target pixel value and the estimated pixel value for each pixel, as shown in equation (1). Similarly, the L_2 loss is defined as the sum of the squared differences between the target pixel value and the estimated pixel value for each pixel, as shown in equation (2).

$$L_1 = \sum_{i=1}^{n} |y_i - f(x_i)| \tag{1}$$

$$L_2 = \sum_{i=1}^{n} (y_i - f(x_i))^2 \tag{2}$$

where y_i denotes the target pixel value, and $f(x_i)$ denotes the estimated pixel value of the network. The L_1 loss aims to minimize the absolute difference between the pixel values of the target image and the estimated image. It is more robust to outliers, as they do not cause particularly large losses and result in small and stable fluctuations. On the other hand, the L_2 loss aims to minimize the squared error between pixel values of the target image and the estimated image. Outlier points have a large impact on the loss, leading to a smoother image.

2.3. Introduction to the dataset

The STORM image data used in this study were obtained from a previous experiment conducted by Chen's team [14]. STORM microscopy was conducted utilizing a Nikon Instruments N-STORM system (Ti-E model). In summary, the setup incorporates an

Agilent MLC400B for laser emission, comprising a red diode laser (647 nm, 300 mW; MPBC), a green solid-state laser (561 nm, 150 mW; Coherent), a blue solid-state laser (488 nm, 200 mW; Coherent), a violet diode laser (405 nm, 100 mW; Coherent), and employs a 100 × NA 1.49 oil immersion lens. The system separates emitted fluorescence through specific filters (FF02-520/28-25, FF01-586/20-25 × 3.5, and FF01-692/40-25; Semrock), capturing it with a back-illuminated EMCCD camera (iXon DU897, Andor). Cell cultures were prepared on eight-well chambered coverglass slides (Thermo Fisher Scientific, 155409). The preparation protocol for STORM mirrors that of confocal microscopy, with an alteration for pRIP3 staining involving methanol fixation at −20 °C for 10 min to minimize background interference. Following fluorescent antibody labeling, specimens were placed in a buffer comprising 50 mM Tris (pH 8.0), 10 mM NaCl, 0.5 mg ml^{-1} glucose oxidase (Sigma, G2133), 40 μg ml^{-1} catalase (Sigma, C40), 10% glucose by weight/volume, and 143 mM β-mercaptoethanol. Single-colour STORM of CF 647 involved irradiation with a 647 nm laser at 2 kW cm^{-2} power density. Dual-colour imaging commenced with CF 647, followed by CF 568 acquisition under 1–3 kW cm^{-2} laser power density. A 405 nm laser was dynamically adjusted during imaging to regulate blinking. For each channel, 10,000–20,000 frames were captured at 70 fps, with reconstructions performed via the NIS-Elements AR software's N-STORM module. Chromatic precision in STORM imaging was maintained through calibration with 100 nm multi-fluorescent beads, following Nikon's chromatic calibration protocol (NIS-Elements AR with an N-STORM module). Frame-to-frame sample drift was adjusted by tracking multi-fluorescent beads (Thermo Fisher Scientific, T7279) or through image correlation techniques. Consistent settings were maintained across all imaging procedures. In the STORM images, each localization appears as a Gaussian peak, its width proportional to the detected photon count.

Employing the above detection systems, the STOMR images of intracellular RIP1 and RIP3 amyloid proteins was obtained. The proteins undergo progressively aggregation from small circular monomers to large rod-like multimers [14]. It is important to note that the cells were not observed in real time. Instead, batches of cells from the same species were observed, each developing different states of RIP1 and RIP3 amyloid aggregation. These batches were stained separately and subsequently observed using N-STORM microscopy to generate the STORM images.

The dataset consists of 54 sets of two-dimensional images, each possessing a resolution of 5330 × 5200 pixels. Gaussian noise and Poisson noise were added to each set of images, which were then cropped into 64 × 64-sized image blocks. The rationale behind adding Poisson and Gaussian noise is that these types of noise are inherently present in the raw data acquired from fluorescence microscopy procedures. Poisson noise, often referred to as shot noise, and Gaussian noise are commonplace in such imaging techniques. Our objective in introducing both Poisson and Gaussian noise is to simulate the authentic noise encountered in STORM microscopy data. This simulation then serves as a foundation for training noise-free images, with the aim of refining denoising algorithms and models. Consequently, this approach is intended to enhance the denoising performance on raw STORM images that contain inherent noise. The comparative experiments are conducted to validate the superiority of our proposed image denoising algorithm over other existing image denoising methodologies.

The noises were added according to a Python-based algorithm, with Poisson noise being introduced first, followed by Gaussian noise. The addition of Poisson noise was facilitated through the np.random.poisson function in the numpy library, applying Poisson noise to each pixel to conform to a Poisson distribution. Gaussian noise was introduced using the skimage.util.random_noise function from the skimage library, adding Gaussian noise to each pixel to achieve a Gaussian distribution. The noise was added separately to each image, subjecting them to the same levels of Poisson and Gaussian noise. Each pixel was subjected to both Poisson and Gaussian noise, where the level of Poisson noise was related to the signal intensity of the image, having a mean of 0. Gaussian noise was randomly applied across any position in the image, with its mean set by our defined parameters. No scaling was applied to the stack of images, and the noise level was independent of the image size. The images used were not the original images from the camera but processed noise-free images, thus devoid of inherent noise. An overlap of 25% was applied between adjacent images, resulting in a total of approximately 610,000 images. For training purposes, approximately 90% of the images were utilized as the training set, while the remaining images were reserved for testing the denoising effectiveness of the model.

2.4. Experiment and Analysis

We input the cropped STORM noise image training set into the neural network described above in this section for supervised learning training, and use Adam optimizer to optimize the parameters of the network model. The training process consists of 100 epochs with a batch size of 64, and an initial learning rate of 0.00005. During training, the learning rate is gradually adjusted using exponential decay.

After training, the denoised STORM images are obtained by applying the trained network to the STORM noisy images from the test set. The denoising operation significantly eliminates the noise the improves the readability of the images, as shown in figure 2. To evaluate the denoising effect of the algorithm on the STORM images, Poisson noise and

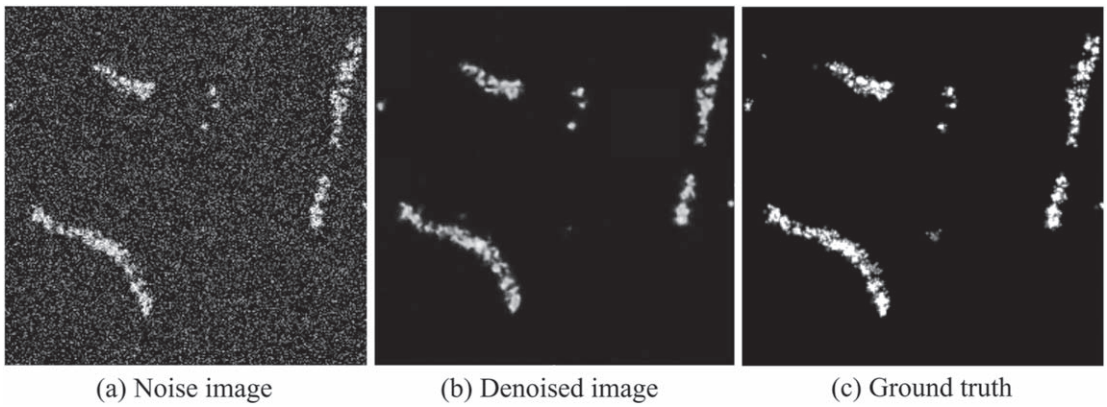

Figure 2. Comparison of denoised image with noisy image and noiseless image. (a) The image after adding noise; (b) The denoised image of the algorithm UNet-Att in this section; (c) The corresponding noise-free image.

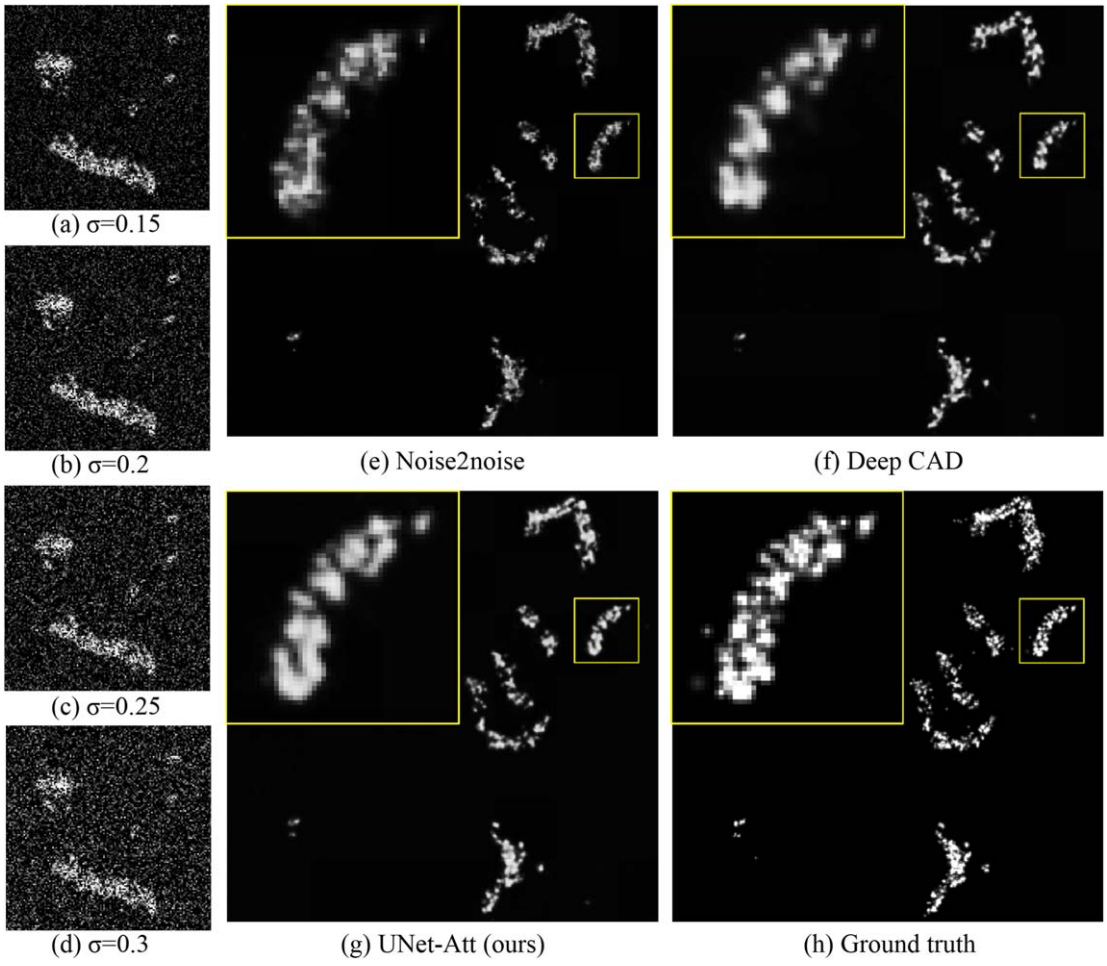

Figure 3. STORM noise images with different levels. The noise image after adding Poisson noise and Gaussian noise with standard deviation of 0.15 (a), 0.2 (b), 0.25 (c), and 0.3 (d); (e) Denoised image using the Noise2noise method; (f) Denoised image using the DeepCAD method; (g) Denoised image using our previously proposed UNet-Att algorithm; (h) The corresponding ground truth image devoid of noise.

multiple levels of Gaussian noise are added to the STORM images in the test set, as shown in figures 3(a)–(d). The denoising results of the algorithm are compared with those of Noise2noise, and DeepCAD algorithms. The comparison is based on the PSNR, SSIM, and MSE values of the denoised results, and the average values of the algorithm models are presented in table 1, table 2, and table 3, respectively. The algorithms UNet-Att achieve better results than the mainstream algorithms at multiple noise levels.

Furthermore, the denoised images with a Gaussian noise level of $\sigma = 0.25$ are visualized and

Table 1. PSNR values of different algorithms at different noise levels (in dB).

σ	Raw	BM3D	Noise2noise	DeepCAD	UNet-Att (ours)
0.15	18.91	23.19	27.10	26.12	**29.38**
0.2	16.69	21.50	26.89	26.89	**29.40**
0.25	14.87	20.01	26.27	27.48	**29.04**
0.3	13.36	18.67	25.64	26.73	**27.56**

Table 2. SSIM values of different algorithms at different noise levels.

σ	Raw	BM3D	Noise2noise	DeepCAD	Att-UNet++ (ours)
0.15	0.99909	0.99945	0.99985	0.99980	**0.99988**
0.2	0.99847	0.99911	0.99985	0.99983	**0.99993**
0.25	0.99766	0.99867	0.99982	0.99986	**0.99992**
0.3	0.99668	0.99814	0.99978	0.99978	**0.99982**

Table 3. MSE values of different algorithms at different noise levels.

σ	Raw	BM3D	Noise2noise	DeepCAD	Att-UNet++ (ours)
0.15	836.7	312.1	124.4	148.3	**92.0**
0.2	1392.5	460.1	131.0	136.4	**71.7**
0.25	2121.1	649.2	151.1	128.6	**79.0**
0.3	3002.7	882.4	175.8	170.5	**134.3**

compared under different algorithms, as shown in figures 3(e)–(h). It can be observed that all algorithms are effective in removing noise, but the ability to recover the original image information varies. Noise2-noise and DeepCAD, although preserving the overall structure of the original image, do not recover the details as well as the algorithm UNet-Att. The algorithm UNet-Att is closer to the original image in terms of detail structure, which performs better than the mainstream algorithms in denoising STORM images in terms of PSNR metric.

3. Image information extraction and clustering processing

After denoising the STORM images, it is necessary to extract information about the proteins present in the images. This information needs to be organized in order to perform statistical analysis and analyze the protein distributions. In the case of the RIP1 and RIP3 amyloid proteins, they exhibit a gradual aggregation process from monomers to multimers within the cell. Additionally, these two proteins tend to cluster together, forming heterodimers. The objective is to extract information about the multimers and then integrate the information from the same multimers using an image information clustering algorithm. Finally, the aim is to quantify the information regarding the heterodimers. Within the domain of image processing, the terms 'particle' and 'cluster' are employed to designate objects of interest. In the context of this study, we use 'particle' to analogously represent what is biologically known as a 'monomer,' and 'multicluster' to correspond to the biological concept of a 'multimer.' This terminology allows us to bridge the understanding between biological structures and their digital representations in image analysis.

3.1. Image information extraction based on Ilastik and ImageJ

After image denoising, the vast majority of noise in the image is eliminated. However, not all the information in the image is relevant to our study. The image contains both free oligomers and multimers, as depicted in figure 4. Our focus is solely to study the state of multimers. Therefore, we aim to eliminate the free oligomers from the image, retaining only the multimers. In this step, we employ Ilastik [40] to perform a dichotomous operation to remove the free oligomers and separate the monomers that cluster into multimers. Ilastik is an interactive machine learning image analysis software, primarily used for tasks such as biomedical image classification, object detection and pixel segmentation.

In Ilastik, we distinguish oligomers and multimers as two different classes of objects, and only keep the multimer objects in the image for the following image processing. As for the multimer objects, each monomer comprising a multimer is separated from each other in the same monomer. The as-obtained output

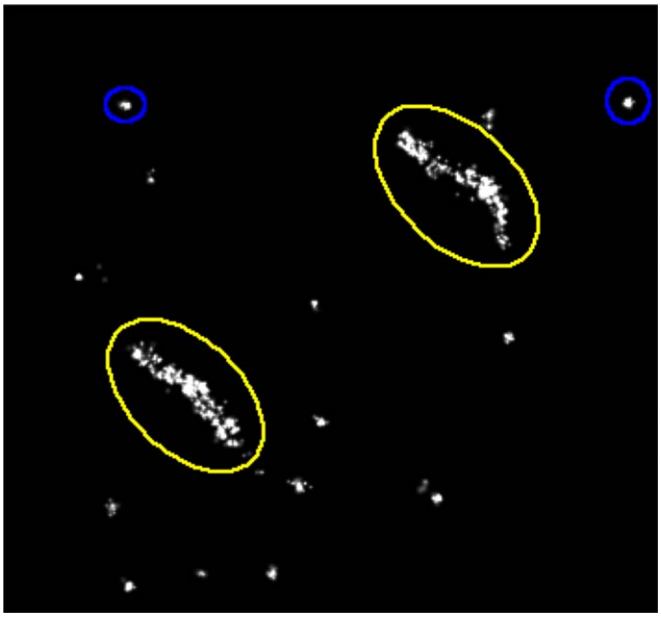

Figure 4. Oligomers and multimers. The substances in the blue circles are oligomers and those in the yellow circles are multimers.

image from Ilastik contain the binarized representations of all individual monomer objects. These are then processed automatically using ImageJ to extract quantitative information [41]. Within ImageJ, each localized monomer is labeled accordingly and analyzed using the 'Measure' function in the ROI Manager interface. The extracted information of each particle comprising the multimers in the STORM images include area, position (measured by Feret parameters), and centroid of each segment within the multimers. This extracted data was stored in a .csv file format. Following the extraction of these comprehensive parameters for each particle, a clustering process is undertaken to facilitate further biological analysis.

3.2. Image clustering algorithm design

After extracting the information of each component of the multimers in the STORM image, direct utilization for biological analysis is unfeasible due to the ambiguity of particle grouping. Consequently, we have developed a clustering algorithm that utilizes image-based information to categorize particles that belong to the same multimer.

Firstly, it is necessary to establish the criteria for determining whether two particles belong to the same multicluster. The most common approach is to consider the distance between the centers of two particles, as implemented by numerous clustering algorithms. However, this method fails to meet our requirements. Since our particles possess distinct areas of varying sizes, it is possible for two particles with a large area and a significant distance between their centers to still belong to the same multimer. Therefore, determining whether two particles belong to the same multimer can not rely solely on the distance between their centers.

To address this challenge, we have introduced a dual assessment of both area and distance. When the centers of two particles are sufficiently close, we can determine that these two particles belong to the same multimer. When the centers of two particles are relatively far apart, but at least one of the particles has a sufficiently large area, the boundaries of the two particles are still very close to each other, and in such cases, it can still be determined that these two particles belong to the same multimer. If either condition is met, it can be concluded that the two particles belong to the same multimer. For a large particle, whose center is far from other particles but whose boundary is close to others, one cannot solely rely on the center distance. Therefore, area is introduced as a metric for distance, mapping area to distance. The relationship between area and distance can be considered quadratic, for example, the area of a circle is πr^2 (r, radius of the circle).

Specifically, if the distance between the centers of two particles is less than a certain threshold value or the distance between their centers is less than a certain fraction of the area distance between the two particles, both conditions indicate that the particles belong to the same multimer. Here the area distance refers to the distance calculated based on the areas of two protein aggregates. After conducting multiple trials, we have established the following expression as the criteria for judging multimer membership:

Consider a multimer Q with a constituent particle denoted as q, that is $q \in Q$. To ascertain if another particle p is identical to q and belongs to the same multimer Q, particle p must satisfy the criteria of

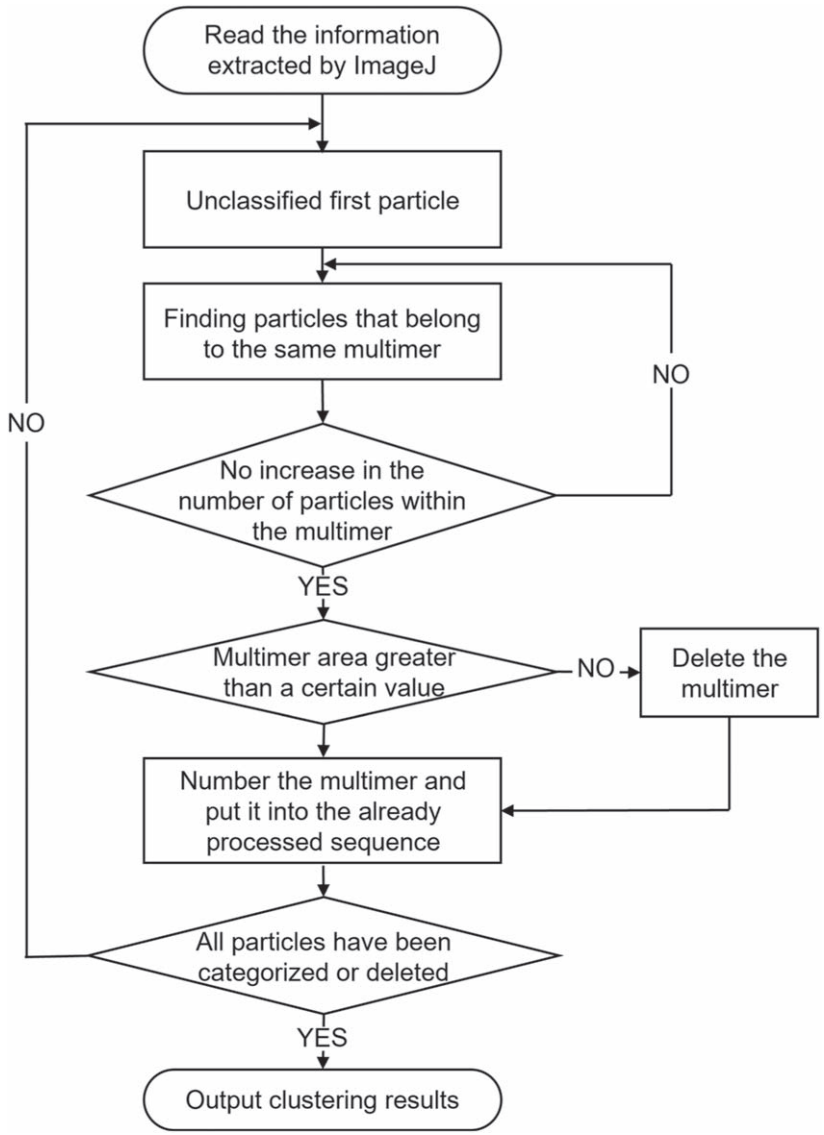

Figure 5. Flowchart depicting the clustering of image information. All particles within the image undergo clustering, and all monomers constituting each multimer are identified through iterative cycling.

equation (3), indicating $p \in Q$:

$$(d_{pq} < d)\mathrm{V}(d_{pq} < D_{pq}) \tag{3}$$

In equation (3), the d_{pq} denotes the distance between the centers of particles p and q, comprising both the transverse distance $d_{pq,x}$ (defined as $|p_x - q_x|$) and the longitudinal distance $d_{pq,y}$ (defined as $|p_y - q_y|$). p_x and p_y denote the x-coordinates, and q_x and q_y the y-coordinates, of the centers of particles p and q, respectively. Both distances must be less than a threshold value d. This threshold d is the maximum allowable center-to-center distance, which would influence the clustering effectiveness and is adjustable for different data sets. D_{pq} represents the area distance between particles p and q, based on the area encompassing them. On account of the quadratic relationship, mapping area to distance involves taking the square root of the area and then multiplying by a constant coefficient, which leads a definition of D_{pq} as $c\cdot\sqrt{\max(s_p, s_q)}$ (c, constant). The terms s_p and s_q represent the areas of particles p and q, respectively. After numerous experiments, the coefficient c has been determined to be 2, which yields the most accurate clustering results for the datasets of RIP1 and RIP3.

The criteria established in equation (3) could serve as a universal method. The parameters set here for the specific datasets of RIP1 and RIP3 within this method have been adjusted through numerous trials to match the characteristics of the RIP1 and RIP3 datasets. If applied to different datasets, adjustments to the parameters (such as the threshold value 'd' in equation (3) and the constant coefficient in the definition of D_{pq}) can be made accordingly.

The algorithm for determining whether two particles belong to the same multimer enables the categorization of all particles within an image. The algorithm was implemented using the python code available at

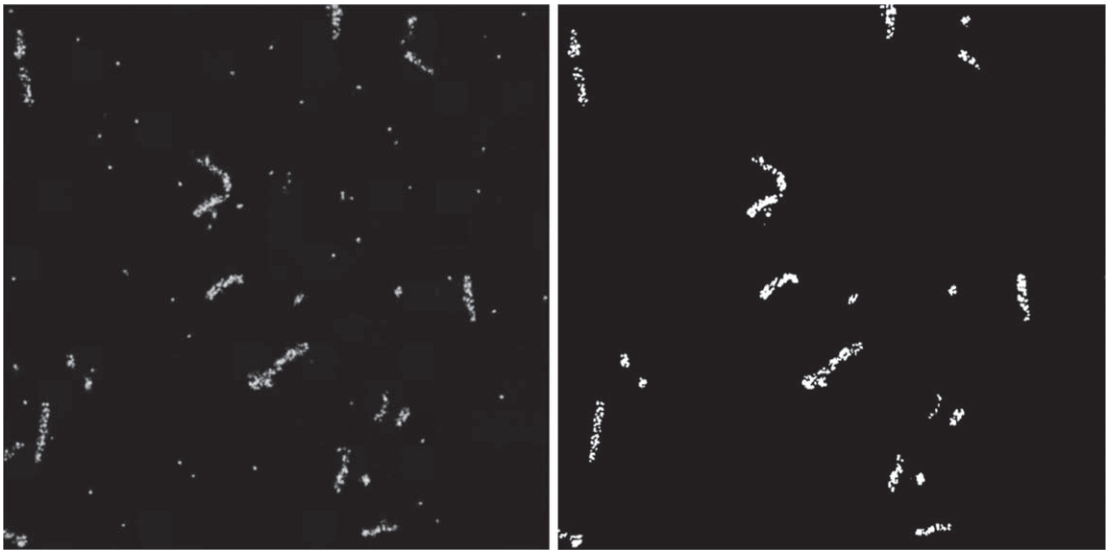

Figure 6. Comparison of images pre- and post-Ilastik processing. The left image shows the pre-processed state; the right image demonstrates the outcome following Ilastik's binary classification processing.

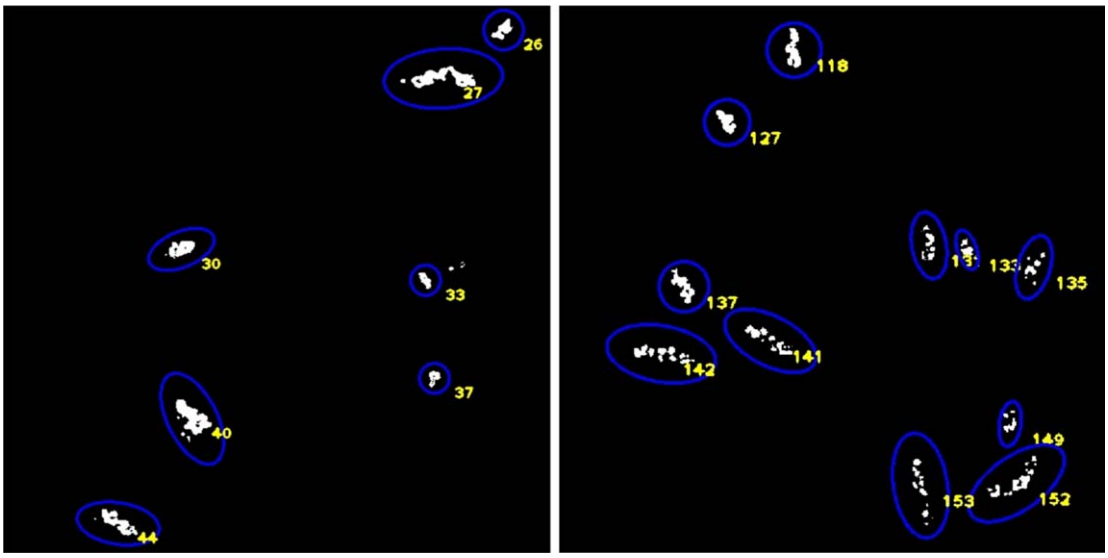

Figure 7. Visualization of image information clustering. Each blue circle represents a multicluster, and the yellow number in the lower right corner of each circle is the numbering of the labeled multicluster.

Table 4. TPR / FPR of the clustering results for various thresholds.

Threshold value	14	16	18	20	22	24
TPR/FPR	82.53%/16.54%	81.78%/16.67%	87.36%/9.96%	91.82%/5.00%	84.39%/11.67%	76.21%/18.97%

the following URL: https://github.com/YongfaYing/STORMing-the-necrosome/tree/main/STORMing-the-necrosome-for-2C-STORM-readout. The procedural flow of the algorithm is outlined below and is illustrated in figure 5:

(1) Read the data file extracted by ImageJ and select the first particle that is not categorized. Identify all particles associated with the same multimer, group them into the same category, and record all the particles that have been categorized.

(2) Sequentially select remaining particles within the multimer, locate associated particles, classify them into the same group, and label them accordingly. Repeat this process until no additional particles are found to associate with this multimer.

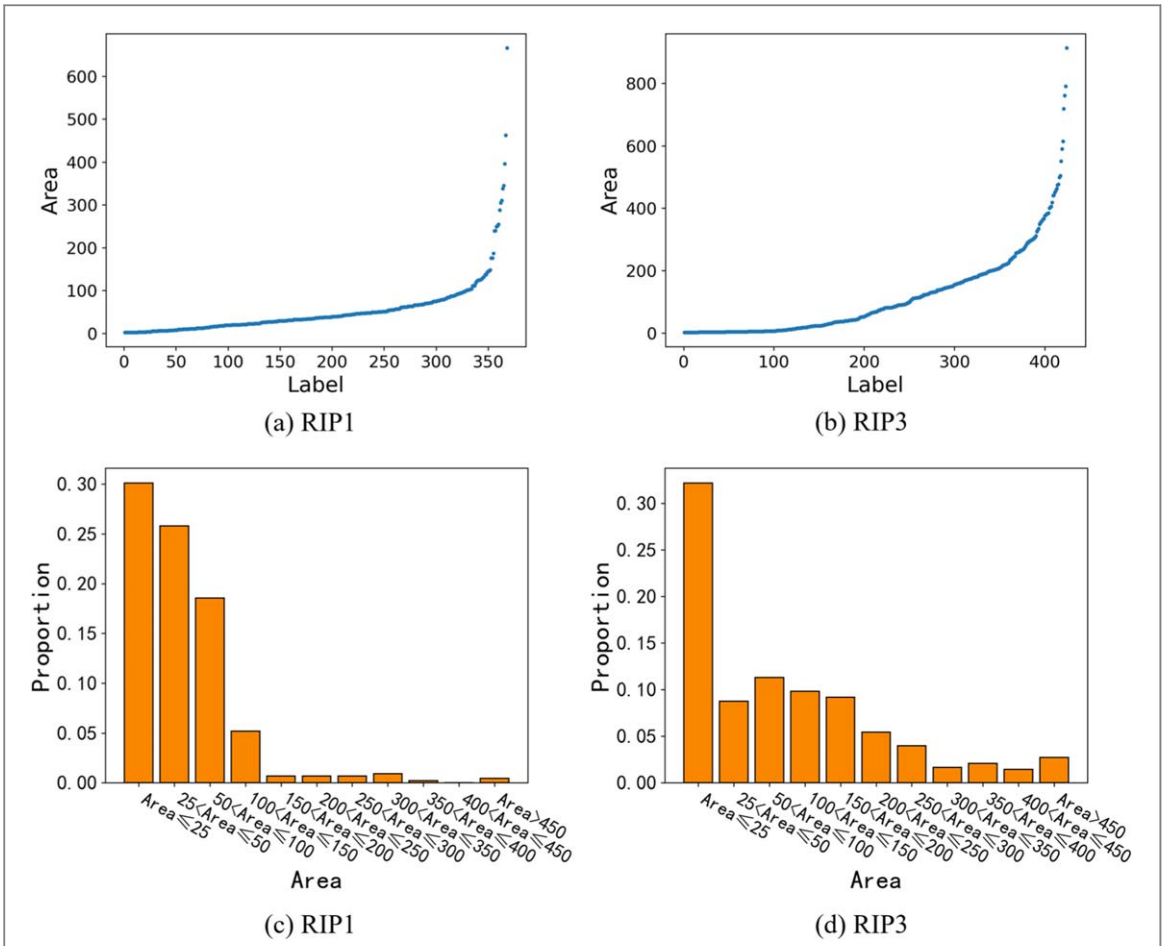

Figure 8. Area statistics of monomers in the multimers. (a)The area distribution of monomers of all constituent multimers in protein RIP1; (b) The area distribution of monomers of all constituent multimers in protein RIP3; (c) The percentage distribution of the area of monomers of constituent multimers in protein RIP1; (d) The percentage distribution of the area of monomers of constituent multimers in protein RIP3.

(3) Calculate the total area of all particles within the multimer. If the combined area is below a predefined threshold, the collection is considered a residual oligomer rather than a multimer and is subsequently excluded.

(4) Continue the cycle of steps (1) to (3) until all particles have been classified or removed.

3.3. Results and analysis

3.3.1. Homologous multimers

The STORM images containing homologous multimers were processed using Ilastik, with the outcomes presented in figure 6. It is evident that post-Ilastik processing, extraneous oligomers in the STORM images are substantially reduced, while the morphology of the multimers is predominantly preserved.

Subsequently, ImageJ was utilized to extract quantitative details such as the area and centroid of each segment within the multiclusteral structure from the STORM images, which were then saved in a csv format. The data pertaining to each multimer segment were amalgamated using the clustering algorithm described in section 3.2, effectively grouping segments belonging to the same multimer. By comparing the true positive rate (TPR) and the false positive rate (FRP) of the clustering result under different threshold values d in equation (3), the threshold for the data used in this experiment was set to an optimal value of 20, which yields the highest accuracy in the clustering outcome (table 4). The TPR refers to the proportion of correctly classified clusters in the clustering results, while FRP refers to the proportion of incorrectly classified clusters. The visualization of the clustering outcomes was demonstrated in figure 7. Following the clustering and integration of image data, statistical analyses were performed on the multimer attributes. For instance, the distribution of monomer areas in the STORM images is illustrated in figure 8 The majority of RIP1 monomers, constituting the largest fraction, are less than 25 pixels in size, with approximately 75% under 100 pixels, suggesting that most RIP1 monomers are relatively small. Similarly, the RIP3 monomers predominantly occupy an area less than 25 pixels, with around 50% under 100 pixels, indicating that a significant portion of RIP3 monomers also exhibit small dimensions.

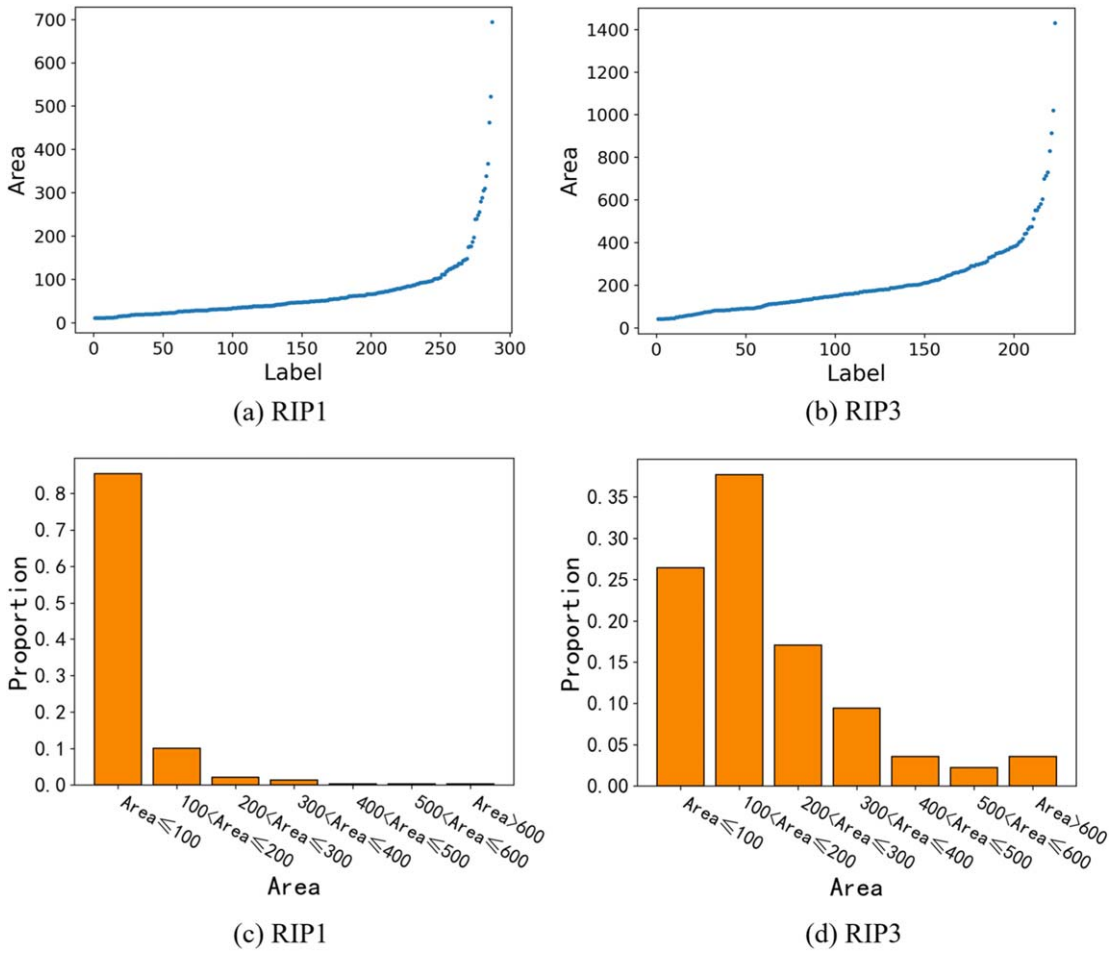

Figure 9. Quantitative area analysis of multimers. (a) The area distribution of multimers in protein RIP1; (b) The area distribution of multimers in protein RIP3; (c) The area percentage composition of multimers in protein RIP1; (d) The area percentage composition of multimers in protein RIP3.

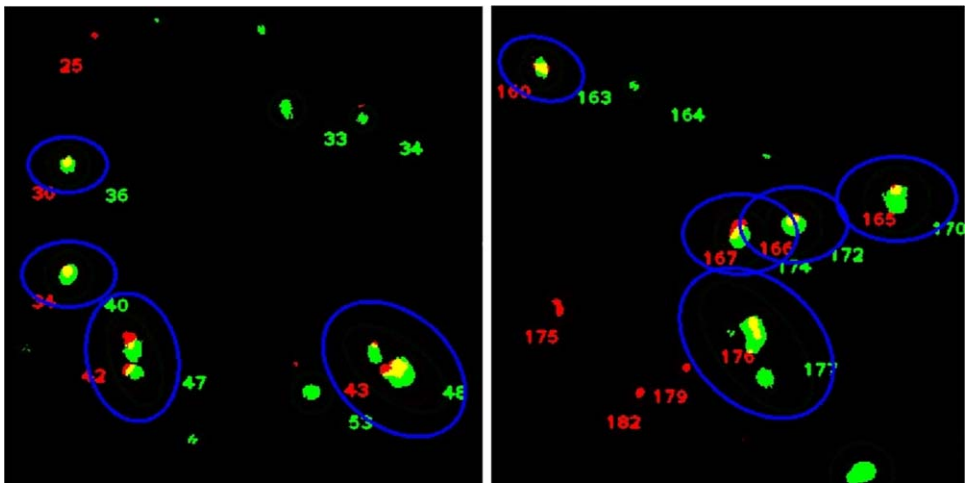

Figure 10. Visualization of heterodimers. Each blue circle indicates an identified heterodimer; red signifies the RIP1 protein with corresponding multimer counts denoted in red; green signifies the RIP3 protein with corresponding multimer counts in green; yellow highlights the overlap between RIP1 and RIP3. The numbers in red and green indicate the label number of the identified RIP1 and RIP3, respectively.

After clustering the image information, the information of the various parts of the multimers is integrated, and we can do statistical analysis of the various information of the multimers. For example, the area of the monomers in the STORM image is shown in figure 8, and the largest percentage of the monomers

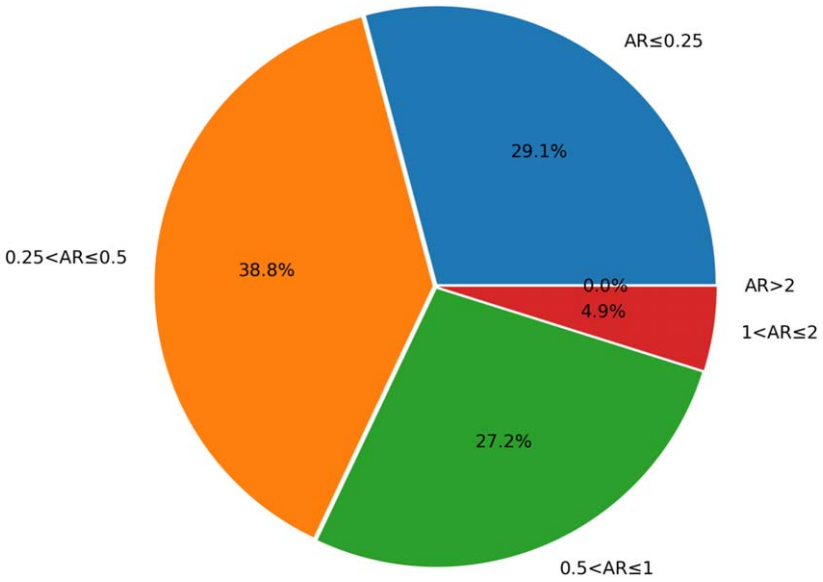

Figure 11. Ratio of the area of the two proteins of the heterodimer. AR indicates the ratio of RIP1 area to RIP3 area.

in the RIP1 image is less than 25 pixels, and about 75% of the monomers are less than 100 pixels, indicating that most of the RIP1 monomers are small. The largest proportion of the area of each part of the monomers that make up the multimers in the protein RIP3 image is also the part with an area of less than 25 pixels, and about 50% of the monomers have an area of less than 100 pixels, indicating that the area of the larger part of the RIP3 monomers is also small.

Additional statistical investigations were conducted on the polymerization areas of the multimers in the images, as shown in figure 9. The data reveal that the predominant polymerization area for RIP1 multimers ranges from 0 to 100 pixels, whereas for RIP3 multimers, it spans from 100 to 200 pixels, signifying that RIP3 multimers tend to occupy a relatively larger polymerization area.

3.3.2. Heterodimers

In the above section, we conducted a detailed examination of the morphological features of protein multimers located at the junction of two overlapping proteins. This investigation was facilitated by employing Ilastik for the segmentation and binarization of multimer objects within images. Following this, ImageJ was utilized to extract pertinent information from these segmented images. The extracted data then underwent a clustering process, focusing specifically on the two proteins that form the heterodimer. This methodological approach enabled us to precisely analyze and understand the complex interactions and structural characteristics of protein multimers.

Our clustering algorithm could also identify colocalized RIP1 and RIP3 and calculate their area ratios. By analyzing the clustered data, we determined the centroid coordinates of the multimers, which facilitated the identification of heterodimers within the images. This identification was achieved by verifying the overlap of the two protein multimers using equation (3) and examining their associated data. The results of this analysis were visualized and annotated directly on the images of the multimeric proteins, as illustrated in figure 10. Within these images, the proteins were represented in separate channels, distinguished by color coding: red for RIP1 protein and its homomultimers, indicated by red numerals; green for RIP3 protein and its homomultimers, indicated by green numerals; and yellow for the regions where RIP1 and RIP3 overlap.

Upon confirmation of heterodimer formation, we quantified the constituent multimers and extracted their morphological data. Subsequently, we performed statistical analyses on this data to elucidate the characteristics of heterodimer aggregation. For instance, we calculated the area ratios of RIP1 to RIP3 in all heterodimers within STORM images, as demonstrated in figure 11. This analysis revealed that the area ratio of RIP1 to RIP3 in heterodimers was greater than that of RIP3 alone in only 4.9% of instances. Moreover, in over half of the heterodimers, the area ratio of RIP1 to RIP3 ranged from 0 to 0.5, suggesting that RIP3 likely plays a dominant role in heterodimer polymerization.

4. Conclusion

In this work, we initially apply our previously proposed denoising algorithm for fluorescent microscopic image denoising to denoise STORM images, and then propose a suite of automated image processing algorithms for information extraction and analysis of image data, incorporating a novel image information clustering algorithm. We construct the

image denoising algorithm UNet-Att and employ supervised learning training to train the network model. The trained network model is then used for denoising prediction, and we compare its performance with other mainstream image denoising algorithms in the field. The results demonstrate the superior effectiveness of our denoising algorithm in the application of STORM image denoising. Following the denoising process, we proceed with the information extraction procedure on the denoised image. Firstly, we utilize Ilastik for the binary classification operation on the image. Subsequently, we employ ImageJ to analyze the particle size in the image, enabling us to extract particle information. Finally, utilizing the image information clustering algorithm we devised in this work, we cluster the fragmented particle information, facilitating statistical analysis of the information contained in the STORM images.

The network architecture of the denoising algorithm in this study is more complicated and intricate, resulting in a trade-off for increased processing time. Moreover, the image clustering algorithm employed in the information extraction algorithm prioritizes clustering accuracy over time cost. Nonetheless, the complete automation of this image processing workflow, from the raw STORM image to the ultimate data analysis, markedly enhances the efficiency of handling large-scale datasets on the whole, as well as the accuracy of data analysis.

Acknowledgment

This work is supported by the National Natural Science Foundation of China under Grant 12090052, Ministry of Science and Technology of the People's Republic of China (STI2030-Major Projects 2021ZD0201900), Wenzhou Institute, University of Chinese Academy of Sciences' startup fund (Grant No. WIUCASQD2023007), Wenzhou Institute, University of Chinese Academy of Sciences' startup fund (Grant No. WIUCASQD2022010).

Data availability statement

The data that support the findings of this study are available upon reasonable request from the authors. https://dropbox.com/scl/fi/0e0fmq4fqb4i8ukj18xnw/dataset.zip?rlkey=m0n7geyz5teczwgcg8rte84i4&st=u3jgselw&dl=0.

Conflicts of interest

The authors declare that the research was conducted in the absence of any commercial or financial relationships that could be construed as a potential conflict of interest.

ORCID iDs

Jianwei Shuai https://orcid.org/0000-0002-8712-0544
Jinjin Zhong https://orcid.org/0000-0002-9782-9354

References

[1] Rust M J, Bates M and Zhuang X 2006 Sub-diffraction-limit imaging by stochastic optical reconstruction microscopy (Storm) *Nat. Methods* **3** 793–6
[2] Huang B *et al* 2008 Three-dimensional super-resolution imaging by stochastic optical reconstruction microscopy *Science* **319** 810–3
[3] Van de Linde S *et al* 2011 Direct stochastic optical reconstruction microscopy with standard fluorescent probes *Nat. Protoc.* **6** 991–1009
[4] Silva L E V *et al* 2016 Two-dimensional sample entropy: assessing image texture through irregularity *Biomed. Phys. Eng. Express* **2** 045002
[5] Vafajoo A, Salarian R and Rabiee N 2018 Biofunctionalized microbead arrays for early diagnosis of breast cancer *Biomed. Phys. Eng. Express* **4** 065028
[6] Codron P *et al* 2021 Stochastic optical reconstruction microscopy (storm) reveals the nanoscale organization of pathological aggregates in human brain *Neuropathology and Applied Neurobiology* **47** 127–42
[7] Veeraraghavan R and Gourdie R G 2016 Stochastic optical reconstruction microscopy–based relative localization analysis (Storm-Rla) for quantitative nanoscale assessment of spatial protein organization *Molecular biology of the cell* **27** 3583–90
[8] Babcock H, Sigal Y M and Zhuang X 2012 A high-density 3d localization algorithm for stochastic optical reconstruction microscopy *Optical Nanoscopy* **1** 1–10
[9] Doksani Y *et al* 2013 Super-resolution fluorescence imaging of telomeres reveals Trf2-dependent T-loop formation *Cell* **155** 345–56
[10] Liu R *et al* 2017 Three-dimensional superresolution imaging of the ftsz ring during cell division of the cyanobacterium prochlorococcus *MBio* **8** e00657-17
[11] Schlegel J *et al* 2019 Super-resolution microscopy reveals local accumulation of plasma membrane gangliosides at neisseria meningitidis invasion sites *Frontiers in Cell and Developmental Biology* **7** 194
[12] Hazime K S *et al* 2021 Storm imaging reveals the spatial arrangement of transition zone components and ift particles at the ciliary base in tetrahymena *Sci. Rep.* **11** 7899
[13] Blandin A-F *et al* 2021 Gefitinib induces egfr and $\alpha5\beta1$ integrin co-endocytosis in glioblastoma cells *Cell. Mol. Life Sci.* **78** 2949–62
[14] Chen X *et al* 2022 Mosaic composition of Rip1–Rip3 signalling hub and its role in regulating cell death *Nat. Cell Biol.* **24** 471–82
[15] Li X *et al* 2022 Caspase-1 and gasdermin D afford the optimal targets with distinct switching strategies in Nlrp1b inflammasome-induced cell death *Research* 9838341
[16] Li X *et al* 2021 Rip1-dependent linear and nonlinear recruitments of caspase-8 and Rip3 respectively to necrosome specify distinct cell death outcomes *Protein & Cell* **12** 858–76
[17] Chaux C, Blanc-Féraud L and Zerubia J 2007 Wavelet-based restoration methods: application to 3d confocal microscopy images *Wavelets XII* (SPIE) pp 140–50 67010E
[18] Klar T A, Engel E and Hell S W 2001 Breaking abbe's diffraction resolution limit in fluorescence microscopy with stimulated emission depletion beams of various shapes *Phys. Rev.* E **64** 066613
[19] Weigert M *et al* 2018 Content-aware image restoration: pushing the limits of fluorescence microscopy *Nat. Methods* **15** 1090–7

[20] Shroff H *et al* 2008 Live-cell photoactivated localization microscopy of nanoscale adhesion dynamics *Nat. Methods* **5** 417–23
[21] Icha J *et al* 2017 Phototoxicity in live fluorescence microscopy, and how to avoid it *Bioessays* **39** 1700003
[22] Helmerich D A *et al* 2021 Photoblueing of organic dyes can cause artifacts in super-resolution microscopy *Nat. Methods* **18** 253–7
[23] Bondani M *et al* 2007 Sub-shot-noise photon-number correlation in a mesoscopic twin beam of light *Phys. Rev. A* **76** 013833
[24] Boyat A and Joshi B K 2013 Image denoising using wavelet transform and median filtering *2013 Nirma University Int. Conf. on Engineering (NUiCONE)* (IEEE) pp 1–6
[25] Mannam V *et al* 2022 Real-time image denoising of mixed Poisson–Gaussian noise in fluorescence microscopy images using ImageJ *Optica* **9** 335–45
[26] Buades A, Coll B and Morel J-M 2005 A non-local algorithm for image denoising *2005 IEEE Computer Society Conference on Computer Vision and Pattern Recognition (CVPR'05)* (IEEE) pp 60–5
[27] Dabov K *et al* 2007 Image denoising by Sparse 3-D transform-domain collaborative filtering *IEEE Trans. Image Process.* **16** 2080–95
[28] Azad R *et al* 2023 Advances in medical image analysis with vision transformers: a comprehensive review *Med. Image Anal.* **91** 103000
[29] de Haan K *et al* 2019 Deep-learning-based image reconstruction and enhancement in optical microscopy *Proc. IEEE* **108** 30–50
[30] Yao B *et al* 2020 Image reconstruction with a deep convolutional neural network in high-density super-resolution microscopy *Opt. Express* **28** 15432–46
[31] Tehrani K F *et al* 2015 Adaptive optics stochastic optical reconstruction microscopy (ao-storm) using a genetic algorithm *Opt. Express* **23** 13677–92
[32] LeCun Y, Bengio Y and Hinton G 2015 Deep learning *Nature* **521** 436–44
[33] Hu H *et al* 2023 Modeling and analyzing single-cell multimodal data with deep parametric inference *Briefings Bioinform.* **24** bbad005
[34] Zhao J *et al* 2023 Predicting potential interactions between lncrnas and proteins via combined graph auto-encoder methods *Briefings Bioinform.* **24** bbac527
[35] He Q *et al* 2023 Dear-diaxmbd: deep autoencoder enables deconvolution of data-independent acquisition proteomics *Research* **6** 0179
[36] Lehtinen J *et al* 2018 Noise2noise: learning image restoration without clean data *International Conference on Machine Learning* (PMLR) pp 2965–74
[37] Li X *et al* 2021 Reinforcing neuron extraction and spike inference in calcium imaging using deep self-supervised denoising *Nat. Methods* **18** 1395–400
[38] Zanacchi F C *et al* 2019 Quantifying protein copy number in super resolution using an imaging-invariant calibration *Biophys. J.* **116** 2195–203
[39] Prescher J *et al* 2015 Super-resolution imaging of escrt-proteins at hiv-1 assembly sites *PLoS Pathog.* **11** e1004677
[40] Berg S *et al* 2019 Ilastik: interactive machine learning for (Bio) image analysis *Nat. Methods* **16** 1226–32
[41] Zhong J *et al* 2022 Assembly of guanine crystals as a low-polarizing broadband multilayer reflector in a spider, phoroncidia rubroargentea *ACS Appl. Mater. Interfaces* **14** 32982–93